

Comparison of X-ray and optical measurements in the near-field of an optically dense coaxial air-assisted atomizer

Julie K. Bothell^{a,*}, Nathanael Machicoane^b, Danyu Li^a, Timothy B. Morgan^a,
Alberto Aliseda^b, Alan L. Kastengren^c, Theodore J. Heindel^a

^a Center for Multiphase Flow Research and Education, Department of Mechanical Engineering, Iowa State University, Ames, IA, USA

^b Department of Mechanical Engineering, University of Washington, Seattle, WA, USA

^c X-Ray Science Division, Advanced Photon Source, Argonne National Laboratory, Lemont, IL, USA

ARTICLE INFO

Article history:

Received 23 May 2019

Revised 9 January 2020

Accepted 11 January 2020

Available online 13 January 2020

Keywords:

Near-field spray characterization

Shadowgraph

Spray diagnostics

Synchrotron X-ray radiography

X-ray flow visualization

ABSTRACT

Understanding the near-field region of a spray is integral to optimization and control efforts because this region is where liquid break-up and spray formation occurs, setting the conditions under which the spray dynamics evolve under the gas turbulence and droplet inertia. However, the high optical density of this region complicates measurements; thus, it is not yet well characterized. This paper is intended to compare four of the leading experimental techniques that are being used or developed to study the near-field region of a spray. These techniques are shadowgraphy, tube source X-ray radiography, high-speed synchrotron white-beam X-ray imaging, and synchrotron focused-beam X-ray radiography. Each of these methods is applied to a canonical spray, using the same nozzle, under identical flow conditions. Synchrotron focused-beam radiography shows that a time-averaged Gaussian liquid distribution is a valid approximation very near the nozzle, before the core has broken apart. The Gaussian behavior continues as the spray progresses further downstream, showing self-similarity. A spray angle can be defined from the linear spreading of the Gaussian intensity distribution with downstream distance. The spray angle found from shadowgraphy is validated with focused-beam testing. Additionally, a novel method of estimating the intact length of the spray from different X-ray techniques, that uses broadband illumination, is presented.

© 2020 Elsevier Ltd. All rights reserved.

1. Introduction

Coaxial atomizers are of interest in research because of their use as fuel injectors for gas turbines and engines, two-phase chemical reactors, and food processing (Lasheras and Hopfinger, 2000). Spray droplet characterization has been a primary focus of this research, especially in the combustion community (Aggarwal, 1998; Law, 1982). Some of the methods commonly used to study the far-field region of sprays include Laser Doppler Velocimetry (LDV), Phase Doppler Particle Analysis (PDPA), and Particle Image Velocimetry (PIV). However, each of these methods relies on the spray being broken into droplets, and are thus not applicable for studying the near-field region. The near-field region is where instabilities begin to develop, and is of utmost importance because of its role in setting up the primary combustion zone (Lightfoot et al., 2015). Fully characterizing this region is difficult because the thick liquid core reflects most visible light, impeding the use of most

noninvasive measurement methods. Thus, the near-field region has not been studied with the depth and rigor that has been applied to the mid- or far-field region.

Shadowgraphy and back-illuminated imaging are often used for studying sprays (Castrejón-García et al., 2011; Stevenin et al., 2012; Westlye et al., 2017). These visible light techniques are useful in making qualitative assessments about the spray and obtaining a measure of the core length, but it is challenging to estimate accurately other quantitative measurements, such as spray angle. X-ray diagnostics have emerged recently as an alternative to optical diagnostics for studying the near-field region (Heindel, 2018; Linne, 2013). Unlike visible light, X-rays are able to penetrate the dense liquid region, and their attenuation is related to the path length and density of the materials through which they pass. The attenuation can then be used to measure (or estimate if the attenuation is from a broadband source) the quantity of liquid present in the line of sight along the X-ray beam. An additional advantage of X-rays is the mild refraction and diffraction at liquid-gas interfaces, which enhances visualization (Kastengren et al., 2012). Ballistic imaging is another measurement technique that has been

* Corresponding author.

E-mail address: jbothell@iastate.edu (J.K. Bothell).

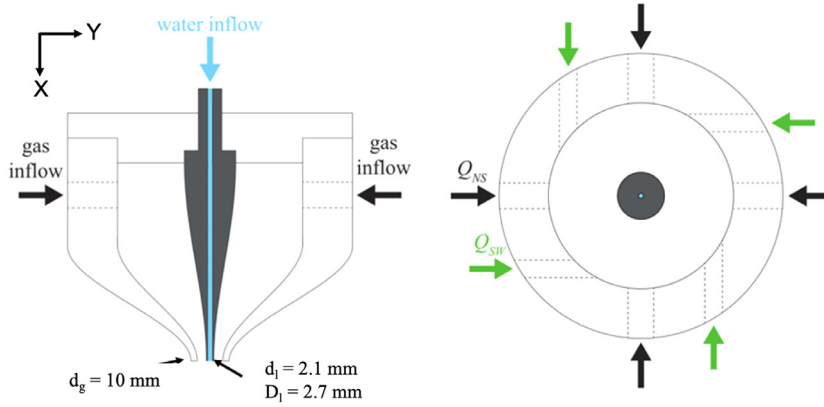


Fig. 1. Nozzle schematic showing liquid and gas inlets of a two-fluid coaxial nozzle. Q_{NS} shows the locations for straight air flow and Q_{SW} shows how swirl air is added (this functionality is not utilized in the current study).

used to investigate the spray near-field (Linne et al., 2009), but is not covered in this study.

To understand how the data from these measurement techniques compare, this study uses an identical experimental setup and flow conditions to provide a side-by-side comparison of multiple techniques. The four techniques used in this study are shadowgraphy (as the visible light technique), tube source X-ray radiography, synchrotron white-beam phase-contrast imaging, and synchrotron focused-beam radiography. Core length and spray angle are the two major defining parameters of the spray near-field that are compared. An accurate measure for the core length was found from shadowgraphy and a method that uses X-ray techniques to estimate this length was developed. The spray angle was found from focused-beam radiography, and the spray angles from the other three methods were compared to this measurement. Additionally, the capabilities, advantages, and disadvantages of each technique are discussed. A complementary study using an impinging jet spray and structured light and 3-D X-ray CT reconstruction was completed by Halls et al. (2013). Using the same impinging jet spray setup, Halls et al. (2014) compared 2-D and 3-D mass distribution measures to focused-beam measurements.

2. Experimental setup

2.1. Nozzle and flow conditions

The nozzle used in these experiments, shown in Fig. 1, is a canonical two-fluid coaxial atomizer (Machicoane et al., 2019). The liquid Reynolds number is defined by:

$$Re_l = (U_l d_l) / \nu_l \quad (1)$$

where $d_l = 2.1$ mm is the inner diameter of the liquid nozzle, ν_l is the kinematic viscosity of the liquid, and U_l is the liquid mean exit velocity, calculated as $U_l = Q_l / A_l$ where Q_l is the liquid flow rate and A_l is the exit area of the liquid nozzle. With $d_l = 2.1$ mm and a liquid nozzle length of 110 mm, the length to diameter ratio is 52 ensuring a fully developed flow. The inner diameter of the gas nozzle at the exit is $d_g = 10$ mm, and the gas Reynolds number is defined by:

$$Re_g = 4Q_{tot} / (\pi d_{eff} \nu_g) \quad (2)$$

where Q_{tot} is the total gas flow rate, and ν_g is the kinematic viscosity of air. The effective inner diameter of the gas nozzle (d_{eff}) is defined as:

$$d_{eff} = (d_g^2 - D_l^2)^{1/2} \quad (3)$$

which is the diameter of a circle with the same exit area as the gas nozzle, and $D_l = 2.7$ mm is the outer diameter of the liquid

Table 1

Gas Reynolds number, momentum flux ratio, Weber number, and mass loading for each condition used in this study.

Re_g	M	We	m
21,200	6.0	40.3	0.55
31,100	12.9	86.8	0.37
46,500	28.9	194.1	0.25
69,300	64.1	430.5	0.17

nozzle. The total gas flow rate is composed of straight and swirl air. As shown in Fig. 1, straight air enters the gas plenum directed at the liquid needle centerline whereas swirl air enters the gas plenum tangent to the plenum wall (which is not used in the current study).

The momentum flux ratio (M) is defined by:

$$M = (\rho_g U_g^2) / (\rho_l U_l^2) \quad (4)$$

where the subscripts g and l define the gas and liquid properties, respectively, and ρ is the fluid density. Additionally, the Weber number (We) and mass loading ratio (m) are defined by:

$$We = \rho_g U_g^2 d_l / \sigma \quad (5)$$

$$m = (\rho_l U_l A_l) / (\rho_g U_g A_g) \quad (6)$$

where σ is the interfacial tension.

All length scales have been nondimensionalized with d_l where appropriate; hence $Y = y/d_l$ is the spanwise coordinate and $X = x/d_l$ is the axial coordinate originating at the nozzle exit. The liquid flow rate is constant for all test conditions considered in this study, yielding a fixed Reynolds number of $Re_l = 1100$ to ensure laminar flow, with a large We and small m to ensure that the breakup and interfacial instabilities are driven by the gas (Lasheras et al., 1998; Lasheras and Hopfinger, 2000). The gas flow conditions selected for this study are summarized in Table 1.

2.2. Shadowgraphy

High-speed back-illuminated imaging and shadowgraphy have been widely used for studying sprays because the interfaces between the liquid and gas regions are easily visible (Castrejón-García et al., 2011; Stevenin et al., 2012; Westlye et al., 2017). The images generally show the entire region of interest of the spray at a high temporal resolution, which enables spatiotemporal analysis of the data. However, it is not possible to capture internal details of

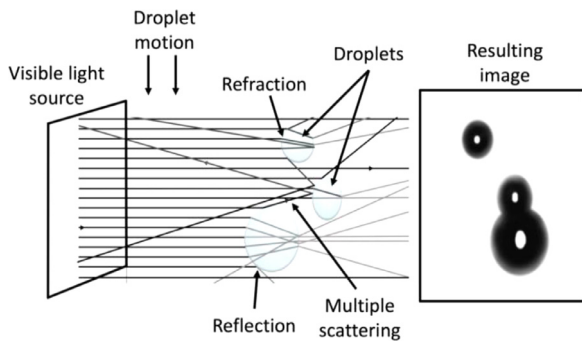


Fig. 2. Shadowgraphy: High-speed imaging using visible light to capture a still shadow of a spray (schematic not to scale).

the spray. Additionally, dense clouds of droplets obscure the light, so they cannot be distinguished from patches of liquid.

Shadowgraphy experiments in this study were conducted using a red light emitting diode (LED) panel, schematically shown in Fig. 2. Although the light coming from this source was not truly parallel, as it would be in shadowgraphy, it has less than 5° divergence so it was considered parallel with negligible error, for simplification in the analysis. As light passes through the spray, it is reflected, refracted, and diffracted away from its original path wherever liquid is present; this creates a shadow in the resulting image. Using a visible light source makes shadowgraphy subject to multiple scattering, also shown in Fig. 2, where the light reflects and diffracts off of multiple droplets, decreasing the sharpness and contrast of the resulting image. The high curvature of droplets also tends to act as a lens, focusing light to the center of the shadow, which results in a bright spot in the center of larger droplets.

2.3. X-ray imaging

Another current method of imaging sprays uses X-rays rather than visible light (Heindel, 2018). The primary advantage of this type of measurement is that the X-rays attenuate (but not reflect and barely refract) as they pass through liquid, greatly reducing refraction and multiple scattering. The resulting images provide internal details of the spray. This study compares the images taken from two types of X-ray producing devices, a tube source and a synchrotron. The two are considered independently because of the difference in how they produce X-rays and the large disparity in the radiation intensity the sources produce, which leads to different types of X-ray measurements.

2.3.1. Tube source X-rays

Tube source X-rays are produced when electrons are accelerated with a high voltage electric field in a cathode ray tube where the electrons impact a metal target (anode) which decelerates the electrons, emitting radiation in the X-ray spectrum. Fig. 3 schematically shows the tube source X-ray setup used in current experiments at Iowa State University's X-ray Flow Visualization Laboratory, which has been described in detail elsewhere (Heindel et al., 2008). The X-ray source has a cone-shaped beam and contains a wide range of photon energies, referred to as broadband X-rays or white-beam X-rays. As the beam propagates through the spray, a fraction of the photons are absorbed by the liquid so that the beam intensity decreases; the decrease is a function of the fluid medium, the amount (path length) of fluid, and the X-ray photon energy. Rather than using the equivalent path length (EPL) of the spray, calculations from tube source radiography use the optical depth values directly which are equivalent to μ^*EPL , where μ is the X-ray attenuation coefficient (Li et al., 2019). Note that μ is a function of the material through which the X-rays pass, as well

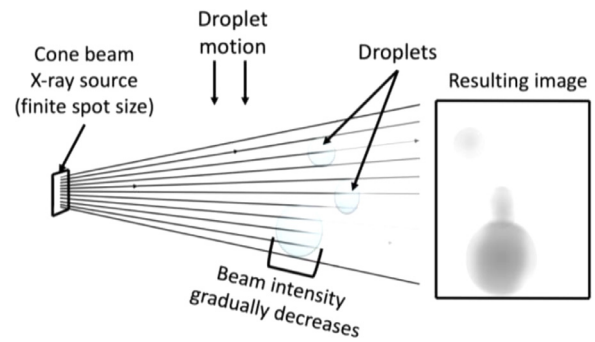


Fig. 3. Tube source radiography: The X-ray beam projects at a cone angle and the intensity decreases in the presence of liquid. The resulting image can be correlated to local projected mass distribution (figure not to scale).

as the wavelength of the X-ray energy, and is typically tabulated for monochromatic X-ray sources, but is a complicated function for polychromatic X-ray sources common in tube sources. The relatively low intensity of the tube source used in this study requires an exposure time of 20 ms, and acquisition speeds of the order of 10 FPS, which are too slow to capture fast-moving events, so the resulting images become blurred. The blurring makes it difficult to interpret individual images, but these can be time-averaged for mean spray measurements. Additionally, the tube source has a relatively large focal spot, which results in a non-negligible penumbra effect (caused by X-rays hitting the same spot on an occluding object from different angles), causing blurred edges. One advantage of the tube source is the larger X-ray beam, which allows the entire spray region to fit inside the beam at one time. The field of view for radiographs in this study was 22.5×26 mm, the tube voltage was 50 keV, and the current was 2.0 mA. More details about the tube source X-ray setup can be found in Heindel et al. (2008) or the setup of Li et al. (2018).

2.3.2. Synchrotron X-rays

The synchrotron beamline used for the measurements in this study was the 7-BM beamline at the Advanced Photon Source at Argonne National Lab; the setup is detailed elsewhere (Kastengren et al., 2012; Heindel, 2018). The synchrotron source provides extremely intense X-rays with an energy range of 5.1–12 keV that are created by fast-moving electrons when they are steered by bending magnets or undulators. Using this X-ray source for radiography of sprays is advantageous because the high X-ray intensity enables microsecond exposures and kilohertz frame rates. This permits the acquisition of time-resolved measurements or images, which allows for the capture of dynamic events and minimizes motion blur. The beam is also highly collimated, which minimizes the penumbra effect, and increases the phase-contrast effect.

2.3.2.1. Synchrotron white-beam imaging. White-beam phase-contrast imaging is named because the beam is not a single wavelength but, instead, uses the broadband emission from the X-ray source. The phase-contrast effect is caused by refraction and Fresnel diffraction where a relatively large propagation distance increases the intensity of phase boundaries. The white-beam phase-contrast X-ray setup is shown in Fig. 4. The beam is highly collimated and the source is approximately 35 m from the test section. The maximum beam size is approximately 6×8 mm. As the beam propagates through the spray, the intensity decreases. This concept is shown for the droplets in Fig. 4 as each of the lines, representing a section of the beam, decreases in intensity depending on the path length of liquid through which it passes. After going through the spray, the beam illuminates a scintillator

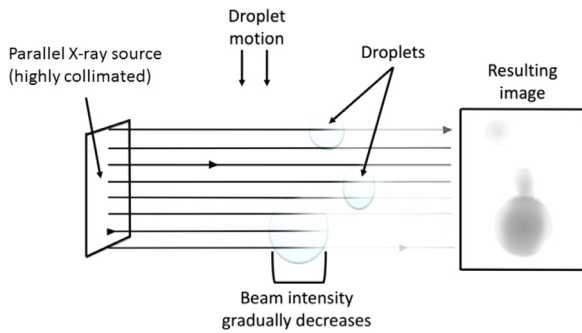


Fig. 4. Synchrotron X-ray imaging: The nearly parallel X-ray beams pass through a spray where the intensity decreases, dependent on the amount of liquid through which they pass. In actual images, the edges are enhanced by a bright region around the droplets (phase-contrast effect, not shown in this figure). The resulting image can be correlated to the local projected mass distribution (figure not to scale).

(not pictured), which creates a visible light image proportional to the incident X-ray intensity. The visible light image is then reflected off a mirror and captured by a high-speed camera. Additional details of white-beam phase-contrast imaging are presented by Heindel (2018).

2.3.2.2. Synchrotron focused-beam radiography. Focused-beam radiography in this study was performed by first filtering the white-beam into a monochromatic beam, and then focusing the beam into a small cross-sectional area of $5 \times 6 \mu\text{m}$ at 8 keV. The resulting beam was then raster-scanned across the spray to acquire line-of-sight measurements. For focused-beam radiography, as the beam passes through the spray, it reduces in intensity in the same way as white-beam imaging. After passing through the spray, the X-ray beam illuminates a PIN diode that produces a voltage, proportional to the beam intensity, which is then recorded. By scanning across the spray, intensity as a function of time signals are recorded at multiple locations. Focused-beam radiography can be highly time-resolved. In this study, focused-beam radiographs are taken at an effective frequency of 270 kHz for 10 s. at each line-of-sight location in the spray.

Because this setup requires the beam to be focused to a small cross-sectional area, the full power of the beam is not required, which enables the use of a nearly monochromatic X-ray beam. This greatly simplifies the subsequent analysis, since X-ray absorption is strongly dependent on X-ray wavelength. A monochromatic beam eliminates beam hardening (preferential absorption of lower energy radiation) so that Beer-Lambert's Law provides an accurate measure of the EPL:

$$EPL = (1/\mu) \ln(I_0/I) \quad (7)$$

where I_0 is the incident beam intensity, I is the beam intensity after passing through the spray, and μ is the X-ray attenuation coefficient. By knowing the X-ray photon energy, the attenuation coefficient can be obtained from the NIST XCOM database (Berger et al., 2010) which is then used to obtain the equivalent path length (EPL). Being able to compute the instantaneous EPL of the liquid makes it possible to measure the mass distribution of the spray, as well as for additional spray dynamic properties to be computed.

The setup for focused-beam radiography is shown in Fig. 5. The inset of the figure shows a representative measured beam intensity over time, changing as the droplets pass through the probe volume. A spherical droplet yields an elliptical curve whose minimum corresponds to its diameter when it is intersected at its center. Droplets that are in the same line of sight result in the superposition of multiple droplets in the measurement, giving more complex

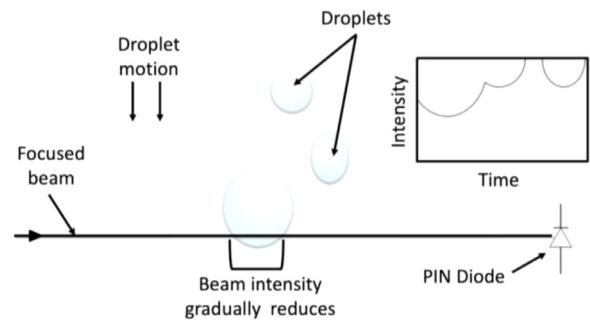


Fig. 5. Focused-beam radiography: Intensity of an X-ray beam, that has been focused down to a small cross-sectional area, decreases following Beer-Lambert's Law as it passes through liquid (figure not to scale).

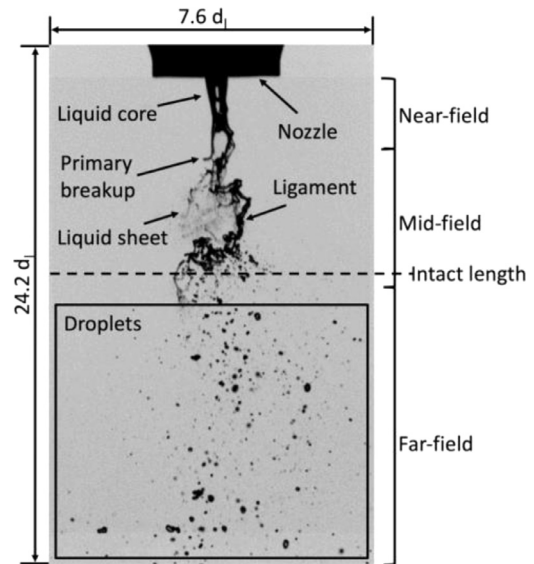


Fig. 6. Instantaneous shadowgraph image from a high-speed spray sequence, taken at $Re_l = 1100$ and $Re_g = 21,200$ with a frame rate of 10 kHz and exposure time of $1 \mu\text{s}$.

results and making it difficult to distinguish the signal from each droplet.

3. Results

3.1. Shadowgraphy

A shadowgraph image of the spray is shown in Fig. 6 where many of the visible spray characteristics are identifiable. The liquid core is nearest to the nozzle and characterized as a continuous section of thick liquid that has not yet broken apart. Primary breakup can be seen, leading to the formation of ligaments and liquid sheets. As ligaments move further downstream, they break up into large droplets while liquid sheets break into smaller droplets. Once the primary breakup process is finished and the liquid moves to the mid-field region, the spray has become more dilute and broken into droplets that continue to split apart as the turbulent gas flow advects them downstream. When using shadowgraphy, large particles can be seen, but their smaller neighbors often go unobserved because of the low contrast at that scale and the insufficient spatial resolution. Additionally, a percentage of smaller droplets is not captured when the light source is not perfectly parallel. The minimum resolvable object size measured for this setup was 0.25 mm.

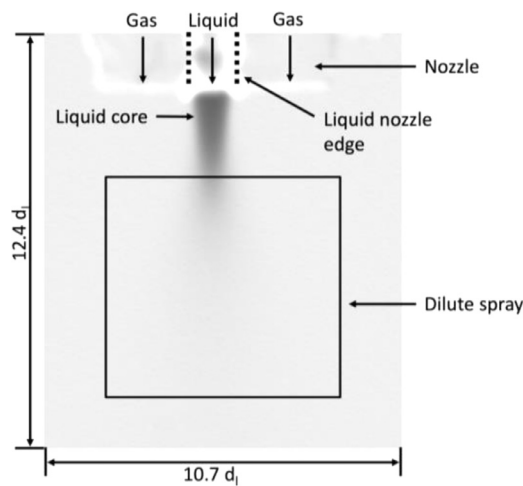


Fig. 7. Tube source X-ray radiograph. Single radiograph normalized to emphasize the spray region showing the liquid mass distribution for the entire flow field region of interest. The momentum flux ratio was 6.0 with an image capture rate of 10 FPS. Gas and liquid conditions are $Re_l = 1100$ and $Re_g = 21,200$.

For this study, from the grayscale shadowgraph, where the background was light and the liquid was dark, image thresholding was used to create a binary image that defined the gas-liquid interface. However, the center region of the liquid droplets and the liquid jet core were lighter or the same intensity as the background because the liquid acted as a lens and focused the illumination; this was corrected through image processing when binarizing the images. A global, bimodal threshold that minimized the weighted within-class variance was applied to all images, which provided binary images with minimized thresholding error. After identifying the location of the liquid, the intact length (longitudinal extent of the instantaneous section of liquid still fully attached to the nozzle) from each image was averaged together. The error in intact length measurements from shadowgraphy images was calculated to be 15% by Charalampous et al. (2016) for a spray with a more dense droplet field, so the experiments here are estimated to have at or below 15% measurement error. The average intact length as determined by shadowgraphy for varying flow rates will be compared to other methods below.

3.2. Tube source X-rays

A time-average tube source X-ray radiograph, representative of the images taken for this study, is shown in Fig. 7. The canonical nozzle is the bright region along the top of the image, and the image has been normalized to emphasize the spray region, which appears as the dark region. The spray in the original tube source radiograph is close to a time-average image because the exposure time of 20 ms is too long compared to the flowfield time scales. The darker regions represent a longer liquid pathlength, and the lighter regions represent less attenuation by the liquid. To increase the contrast between the liquid and the gas background, the liquid was doped with potassium iodide (KI) at a concentration of 20% by mass, which provides measurements with an estimated measurement error of 5%. Past studies have shown that a KI concentration of up to 20% has a negligible effect on the density and viscosity of water, and a KI concentration of 20% by mass does not affect beam hardening (Halls et al., 2014). The image shown in Fig. 7, at a resolution of 327×377 px, covers an area that is $10.7 \times 12.4 d_l$ (22.5×26 mm), and is from a video sequence that was acquired at a rate of 10 FPS using a Photron FastCAM Mini AX50.

A flat-field correction was first used to reduce the fixed noise pattern and then averaged over several seconds, to get a mean pic-

ture of the spray attenuation. The optical depth is used in these measurements because the X-ray attenuation coefficient is not precisely known for the broadband tube source (Li et al., 2019).

3.3. Synchrotron white-beam imaging

Fig. 8 shows several synchrotron white-beam images from locations along or near the centerline of the spray. Each image has an exposure time of $1.05 \mu\text{s}$ and was taken from a series of X-ray images that were captured at a rate of 6 kHz with a Photron FastCAM Mini AX50. The images were taken at different locations along the spray, as the beam size is much smaller than the width of the spray; thus, they could not be taken synchronously. This highlights a notable difference with the tube source X-ray imaging used in this study. The tube source was able to image the spray in its entirety, but at a slower frame rate and lower flux, whereas the synchrotron white-beam imaging provided high-speed high-resolution images but over a smaller field of view. The synchrotron beam was setup for phase-contrast imaging in this study, which enhances the edges of phase differences, making the liquid-gas interface more clearly delineated. However, the analysis presented below does not use the phase-contrast effect, but rather treats the technique as attenuation only imaging.

Unique spray characteristics are distinguished in each image. Unlike shadowgraphy that mostly shows a binary representation of the liquid location, synchrotron X-ray imaging measures the optical depth, which is related to the amount of liquid that is present in the projected image. Hence, the ability to do high-speed X-ray imaging provides more details and highlights many spray features that are not observed with other imaging methods, such as overlapping droplets and liquid features. The liquid core in the spray shown here was more complex than a simple jet with bag formation, as shown in Fig. 6 with shadowgraphy. The phase-contrast image at the nozzle exit ($X = 0.8, Y = 0$) shows the initial formation of bags and ligaments, even before one nozzle diameter away from the nozzle exit plane. Moving downstream ($X = 2.3, Y = 0$), internal structures of the core continue to be seen as bags start to form. Then, the spray begins to form thin liquid sheets and ligaments ($X = 3.8, Y = 1.5$) which break apart as they advect downstream to form small and large droplets, respectively. One particular challenge with high-speed X-ray imaging is that specific flow features are all imaged in the same projection, shown as “stacked features” in Fig. 8 ($X = 6.8, Y = 0$). However, one example of the unique features of this imaging method is the ability to capture air bubbles within the liquid region ($X = 6.8, Y = 0$).

3.4. Synchrotron focused-beam radiography

Synchrotron focused-beam radiography provides an X-ray intensity measurement as a function of time. In this study, an effective signal acquisition rate of 270 kHz over a 10 s. period was recorded at each raster scan location. The instantaneous intensity signal is then used with Beer-Lambert's Law (Eq. (7)) to determine the instantaneous equivalent path length (EPL). Averages at each location were used to obtain contour maps of the spray over the entire flow field. Because data were taken at discrete locations, the data were linearly interpolated to estimate the EPL values between acquisition locations. For the given flow conditions, the maximum EPL was larger than the inner diameter of the liquid nozzle, showing that the liquid spreads out slightly after leaving the nozzle, wetting the outer liquid needle surface, so the initial jet diameter is approximately equal to the outer needle diameter, but still remains intact. This is confirmed by images from synchrotron white-beam phase-contrast imaging (Li et al., 2017). Using the same method as Kastengren et al. (2008), the absorption coefficient in Beer-Lambert's law has an uncertainty of approximately 1.5%, and the

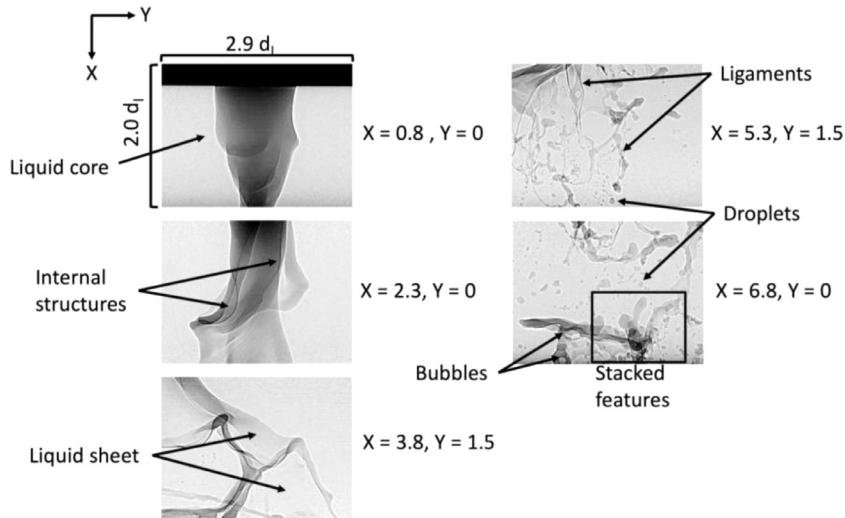


Fig. 8. Synchrotron white-beam X-ray images were taken near, or along the centerline ($Y = 0$) while the X distance increases with $X = 0$ corresponding to the jet exit. X and Y locations were non-dimensionalized by d_i , and identify the image center. $Re_1 = 1100$ and $Re_g = 21,200$ with a capture rate of 6 kHz and an exposure time of 1.05 μ s.

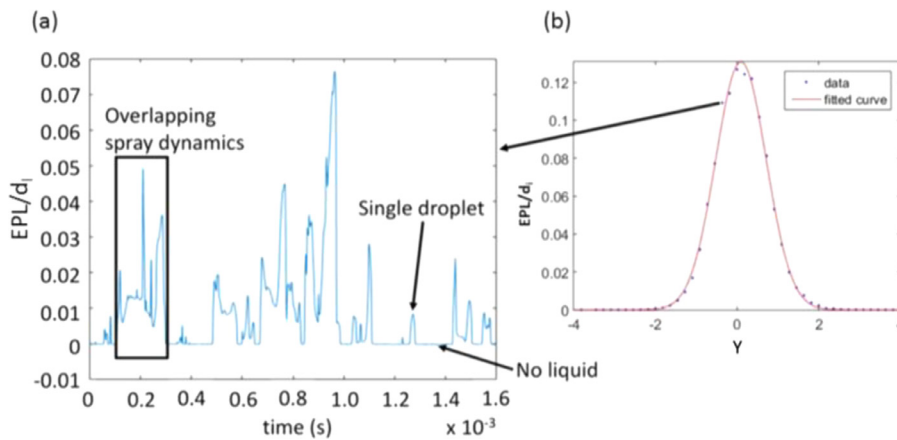


Fig. 9. Focused-beam PIN diode signal, with $Re_1 = 1100$ and $Re_g = 21,200$: (a) a short sample of focused-beam data showing the instantaneous effective path length as a function of time, taken at $X = 2.38$ and $Y = -0.48$ and (b) the average EPL/d_i from one scan across the spray at $X = 2.38$.

measurement positions have an axial uncertainty of $\pm 20 \mu$ m and a spanwise uncertainty of $\pm 5 \mu$ m. The total measurement uncertainty is therefore estimated to be $\pm 3.2\%$.

A sample of the instantaneous EPL from focused-beam data at $(X, Y) = (2.38, -0.48)$ from a short time span (1.6 ms) is shown in Fig. 9a. These data were acquired by raster scanning across the spray and pausing at each data point location for 10 s to collect data, which was long enough to gather good statistical data for the time-varying system. From plots like these, the times when there was no liquid present are evident because the equivalent path length is very near zero. Individual droplets passing through the focused-beam are easily identified by elliptical curves in EPL. For much of the signal, however, the precise spray dynamics are difficult to discern because the signal is composed of several overlapping projected liquid dynamics; one of these regions is identified in Fig. 9a as overlapping spray dynamics.

3.5. Self-similarity

To determine if the spray angle can be accurately described as the angle between two straight lines, it was first necessary to determine if the spray was self-similar and widening in a linear fashion. It has been established that the quantity of liquid present in the cross-sectional area of a spray field can be described by a self-

similar Gaussian curve in the mid-field region (Powell et al., 2000; Yue et al., 2001). The Gaussian distribution follows the velocity in single-phase jets (Van Wissen et al., 2005).

Using focused-beam raster scans that span the width of the spray, a Gaussian curve fit accurately represented the EPL data in the span-wise direction for all cases of the spray that were tested with data that were taken $1d_i$ or farther from the nozzle exit plane. To visualize the self-similarity of the data, the EPL was scaled so that:

$$EPL_{scaled} = EPL(x, y) / EPL(x)_{max} \quad (8)$$

where $EPL(x)_{max}$ was the maximum EPL at each axial (x) location. Additionally, the EPL distributions were scaled for the spray width using the Y location corresponding to 2σ where σ is the standard deviation, so that $y_{scaled} = y / |2\sigma|$. This scaling collapsed all the data, proving self-similarity. A sample of the scaled data for $Re_1 = 1100$ and $Re_g = 21,200$ is shown in Fig. 10a.

3.6. Spray angle comparison

The results from focused-beam radiography, shadowgraphy, and tube source radiography were all used to create a time-averaged spray map. For focused-beam radiography, the average spray map represented the average EPL, as shown in Fig. 10b. For shadowgraphy, the average spray map was an average of binarized images

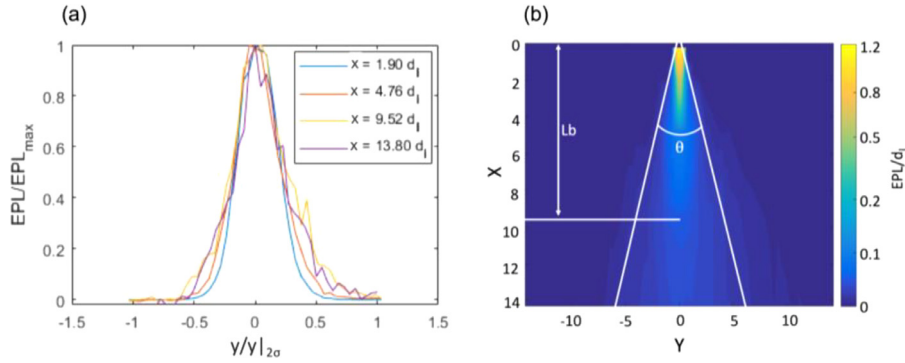


Fig. 10. $Re_g = 1100$ and $Re_l = 21,200$ showing (a) self-similar jet profiles, scaled by EPL_{max} and 2σ , and (b) average EPL/d_l contour map showing the jet spreading angle, θ , and the intact length, L_b .

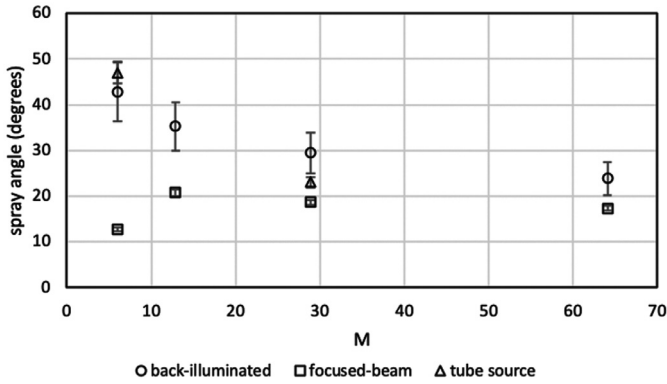


Fig. 11. Comparison of spray angle for multiple testing techniques at varying momentum flux ratios, where the error bars represent the estimated experimental error.

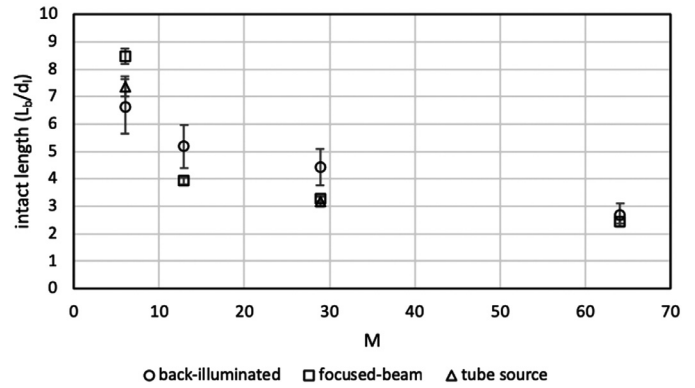


Fig. 12. Comparison of intact length for multiple testing techniques at varying momentum flux ratios, where the error bars represent the estimated experimental error.

representing the probability of the presence of liquid. For tube source X-rays, the average spray map represented the averaged intensity which is linked to the optical depth, and was created after individual images were normalized with the background intensity, shown in Fig. 7. The phase-contrast imaging presented here does not provide sufficient information to calculate the spread angle because the phase-contrast imaging region did not capture the entire spray. Stitching phase-contrast images together was not possible because the incident X-ray flux from the synchrotron varied with time, producing non-uniform background intensities from one imaging region to another. The period of the X-ray flux variance ranged from milliseconds to several hours and developing a method of adjusting images based on the flux variance was beyond the scope of this study.

At any given axial location, a Gaussian curve fit was applied to the data and the y -location of 2σ from the Gaussian curve was defined as the edge of the spray for this study. The spray angle was then defined as the angle between the two lines that connect the 2σ locations. This angle is shown as θ for $M = 6.0$ in Fig. 10b. Using the 2σ location as the spray edge is an arbitrary choice, but is valid for comparison because the angle would scale with the Gaussian distribution so that the spray angle for any σ location could be calculated by multiplying the current spray angle by a constant.

Comparing the spray angle obtained from shadowgraphy, focused-beam radiography, and tube-source radiography gives different results for low gas momentum flux ratios. At higher gas momentum flux ratios, the results are much closer for all three methods, as shown in Fig. 11. At low momentum flux ratios, as the spray progresses further downstream (beyond the measurements from focused-beam radiography) the spray angle increases. This explains

the larger spray angle for shadowgraphy and tube-source radiography, because they both captured a larger spray field of view. As the gas momentum flux ratio increases, the spray angle found from the three methods are more similar because the physical extent of the near-field becomes smaller and the three imaging methods capture the same physics in their different fields of view. This shows that the spray edge at lower momentum flux ratios are not completely straight. Improved measurements would have focused-beam measurements further downstream, to ensure the same spray field for all measurement techniques. The most accurate value of the spray angle is found through focused-beam radiography because of the high precision of the measurements. The angle found from tube-source radiography is more accurate than shadowgraphy since the average map of shadowgraphy shows the presence or not of liquid, rather than the amount of liquid. However, the high correspondence between tube-source measurements and shadowgraphy show that the probability map found from shadowgraphy could be used with acceptable accuracy for finding the spray angle at high momentum flux ratios.

3.7. Intact length comparison

The intact length (L_b) of a spray is defined as the average axial length at which the liquid remains attached to the nozzle. This attachment is either caused by a liquid core or ligaments that remain connected to the liquid at the nozzle tip. The intact length for shadowgraphy ($L_{b,SI}$) was computed by measuring the intact length from a series of images using image processing to determine the longitudinal extend of the liquid core on each instantaneous image. The lengths were then averaged, as shown in Fig. 12, for varying

gas momentum flux ratios. Visual inspection of the intact length from the image series showed minimal error from detached ligaments and droplets that obscured the measurement, even in sprays with higher momentum ratios where droplet clouds are present. For sprays with a denser cloud of droplets surrounding the liquid core, it will often be necessary to estimate the intact length from other measurements, such as X-ray radiography. The method for estimating the intact length is below.

For measurements that use the EPL, the core length has been shown to correlate to the distance where the average EPL along the centerline is 30% of the maximum EPL (EPL_{max}) along the centerline of the particular spray (Lightfoot et al., 2015). It is important to note that the core length and intact length are not the same measure and the core length does not have a consistent definition throughout the literature. However, using the same technique as Lightfoot et al. (2015), a ratio of EPL to EPL_{max} was defined that provides a reasonable estimate of the intact length. For focused-beam radiography, the ratio found that provides the most accurate intact length is $L_{b,FB} = 0.02 * EPL(x_0)_{max}$. The $L_{b,FB}$ ratio was found by determining the EPL value along the centerline, at the intersection of the intact length (as found from shadowgraphy). Because focused-beam radiographs are point measurements, if the intact length location did not lie on a point, the values between points were estimated using a linear fit between the two nearest axial locations. A comparison of the results shows that a good estimate of the intact length was found from focused-beam imaging, shown in Fig. 12.

The same method was used to estimate the intact length from tube-source X-ray images. The ratio of intensity along the centerline was calculated for (I/I_0) as 20% where $L_{b,TS} = 0.20 * I_{max}(x_0)/I_0$, indicating that the threshold may be a function of the X-ray power and spectrum. The resulting intact lengths from this method are shown in comparison to the more direct measurements from shadowgraphy in Fig. 12. The high correspondence between the shadowgraphy and tube-source radiography intact lengths show that the estimate from tube-source radiography was a reasonable estimate.

Phase-contrast images were not used in estimating the intact length because the field of view was too small so the spray had to be imaged in sections. Thus, the core or attached ligaments did not all fit into one imaging frame. Additionally, the differences in the projected intensity between spray regions where the liquid core was intact and where it was broken into a multitude of large liquid droplets made the detection of intact length uncertain. The intensity difference could be magnified in future experiments by doping the liquid with a sensitizer, similar to the KI that was added to the water for tube source X-ray imaging.

4. Discussion

Shadowgraphy required less time for data acquisition because the system was capable of capturing a large portion of the flow field in a single set-up. Unlike X-ray images, shadowgraph images do not show the internal dynamics of sprays or the initial bag and ligament formation, so they can only be used where a binary image showing the outline of the spray will suffice. Shadowgraphy is a great option for obtaining the core length of a spray and an excellent option for initial testing or proof of concept testing to qualitatively assess the spray uniformity.

With tube-source radiography, it was not possible to capture all the same breakup dynamics as with the synchrotron beam or shadowgraphy because a longer exposure was required to account for the low intensity source. However, it was possible to capture the entire spray region in the same image, which was not possible with synchrotron imaging. One of the largest benefits of using a tube-source X-ray setup is the ease of access when compared

to the synchrotron source because it is possible to install a tube-source in a university or industrial lab setting.

Synchrotron phase-contrast imaging works well for qualitative space- and time-resolved analysis of the spray features. The images showed droplet formation, bubbles, ligaments, as well as bag formation and breakup. An image time series (i.e., video) can also show complex breakup events with internal air bubbles (Li et al., 2017). Quantitative measurements from white-beam images are possible but were challenging in this study because of the small intensity differences between the regions with and without liquid, and the inability to correlate objects across imaging regions.

Focused-beam radiography yielded accurate EPL values for the near-field region of the spray. They were also highly time-resolved and were used to find the equivalent path length statistics. However, the line-of-sight measurements do not allow for spatial and temporal information to be acquired at the same time unless the spray is highly repeatable and the data acquisition system is phase-locked (which was not the case in this study). Focused-beam measurements often require another experimental technique such as shadowgraphy or synchrotron white-beam measurements to probe the spray in a complementary way. The mechanisms of breakup can be made evident through imaging and then quantitative statistics from the focused-beam measures can better quantify spray parameters.

5. Conclusions

Using focused-beam radiography, a Gaussian distribution of the EPL was found near the exit plane. The Gaussian behavior continued to exist as the spray progressed downstream with $EPL(x)_{max}$ decreasing and the spray width increasing. Scaling the spray based on the $EPL(x)_{max}$, and the 2σ width of the Gaussian fit as the spray edge, shows the EPL distributions collapsing into a single curve, proving that they are self-similar.

An accurate measure of the spray angle was determined using focused-beam radiography and tube-source radiography. The spray angle from shadowgraph imaging provided similar results to those from focused-beam radiography and tube-source radiography at high gas momentum flux ratios. However, focused-beam radiography showed a smaller spray angle at low gas momentum flux ratios because the angle changes downstream and the spray region that was required to get a reasonable estimate at these conditions was larger than the field of view used in this study for focused-beam radiography. Although the spray angle from shadowgraphy came from a binary distribution of the probability of liquid intercepting the light beam, rather than an average EPL, the results show that it can provide a reasonable estimate of the spray angle.

The intact length was most accurately determined through shadowgraphy. For focused-beam radiography, a threshold value of 2% of the EPL_{max} along the centerline of the jet resulted in a strong correlation with the results from shadowgraphy. The threshold value for tube-source imaging that provided the most accurate intact length is 20% of the I_{max} which also showed good correlation to the intact length from shadowgraphy.

Declaration of competing interest

The authors declare that they have no known competing financial interests or personal relationships that could have appeared to influence the work reported in this paper.

CRediT authorship contribution statement

Julie K. Bothell: Writing - original draft, Formal analysis, Investigation. **Nathanael Machicoane:** Investigation, Writing - review & editing. **Danyu Li:** Investigation. **Timothy B. Morgan:** Investigation.

Alberto Aliseda: Investigation, Writing - review & editing. **Alan L. Kastengren:** Resources, Methodology. **Theodore J. Heindel:** Supervision, Writing - review & editing, Resources.

Acknowledgments

This work was sponsored by the Office of Naval Research (ONR) as part of the Multidisciplinary University Research Initiatives (MURI) Program, under grant number N00014-16-1-2617. The views and conclusions contained herein are those of the authors only and should not be interpreted as representing those of ONR, the U.S. Navy or the U.S. Government.

A portion of this work was performed at the 7-BM beamline of the Advanced Photon Source, a U.S. Department of Energy (DOE) Office of Science User Facility operated for the DOE Office of Science by Argonne National Laboratory under Contract No. DE-AC02-06CH11357.

The tube source X-ray work was completed in the X-ray flow visualization facility at Iowa State University, which was developed with support from the National Science Foundation under award number CTS-021637 and Iowa State University.

References

- Aggarwal, S.K., 1998. A review of spray ignition phenomena: present status and future research. *Prog. Energy Combust. Sci.* 24 (6), 565–600.
- Berger, M.J., Hubbell, J.H., Seltzer, S.M., Chang, J., Coursey, J.S., Sukumar, R., Zucker, D.S., Olsen, K., 2010. XCOM: Photon Cross Section Database. National Institute of Standards and Technology, Gaithersburg, MD (version 1.5). [Online] Available: <http://physics.nist.gov/xcom>.
- Castrejón-García, R., Castrejón-Pita, J.R., Martín, G.D., Hutchings, I.M., 2011. The shadowgraph imaging technique and its modern application to fluid jets and drops. *Rev. Mex. Fis.* 57 (3), 266–275.
- Charalampous, G., Hadjiyiannis, C., Hardalupas, Y., 2016. Comparative measurement of the breakup length of liquid jets in airblast atomizers using optical connectivity, electrical connectivity and shadowgraphy. *Measurement* 89, 288–299.
- Halls, B.R., Heindel, T.J., Kastengren, A.L., Meyer, T.R., 2014. Evaluation of X-ray sources for quantitative two- and three-dimensional imaging of liquid mass distribution in atomizing sprays. *Int. J. Multiphase Flow* 59, 113–120.
- Halls, B., Radke, C., Heindel, T., Lohry, W., Zhang, S., Meyer, T., Gord, J., 2013. Characterization of three-dimensional dense spray visualization techniques. In: 51st AIAA Aerospace Sciences Meeting including the New Horizons Forum and Aerospace Exposition, p. 477.
- Heindel, T.J., Gray, J.N., Jensen, T.C., 2008. An X-ray system for visualizing fluid flows. *Flow Meas. Instrum.* 19 (2), 67–78.
- Heindel, T.J., 2018. X-ray imaging techniques to quantify spray characteristics in the near-field. *At. Sprays* 28 (11), 1029–1059.
- Kastengren, A., Powell, C.F., Arms, D., Dufresne, E.M., Gibson, H., Wang, J., 2012. The 7 BM beamline at the APS: a facility for time-resolved fluid dynamics measurements. *J. Synchrotron Radiat.* 19 (4), 654–657.
- Kastengren, A.L., Powell, C.F., Riedel, T., Cheong, S.-K., Im, K.-S., Liu, X., Wannig, Y.J., Wang, J., 2008. Nozzle geometry and injection duration effects on diesel sprays measured by X-Ray radiography. *J. Fluids Eng.* 130 (4), 041301.
- Lasheras, J.C., Hopfinger, E.J., 2000. Liquid jet instability and atomization in a coaxial gas stream. *Ann. Rev. Fluid Mech.* 32 (1), 275–308.
- Lasheras, J.C., Villermaux, E., Hopfinger, E.J., 1998. Break-up and atomization of a round water jet by a high-speed annular air jet. *J. Fluid Mech.* 357, 351–379.
- Law, C.K., 1982. Recent advances in droplet vaporization and combustion. *Prog. Energy Combust. Sci.* 8 (3), 171–201.
- Li, D., Bothell, J.K., Morgan, T.B., Heindel, T. J., Aliseda, A., Machicoane, N., Kastengren, A.L., 2017. High-speed X-ray imaging of an airblast atomizer at the nozzle exit. 7th Annual Meeting of the American Physical Society Division of Fluid Dynamics Denver, Colorado, November 19–21 doi:10.1103/APS.DFD.2017.GFM.V0026.
- Li, D., Bothell, J. K., Morgan, T. B., Heindel, T. J., Aliseda, A., Machicoane, N., & Kastengren, A. L., Quantitative analysis of an airblast atomizer near-field region using broadband and narrowband X-ray sources, ICLASS 2018, 14th Triennial International Conference on Liquid Atomization and Spray Systems, Chicago, Illinois, July 22–26, 2018, Submission-ID: 141.
- Li, D., Bothell, J.K., Morgan, T.B., Machicoane, N., Aliseda, A., Kastengren, A.L., Heindel, T.J., 2019. Time-averaged spray analysis in the near-field region using broadband and narrowband X-ray measurements. *At. Sprays* 29 (4), 331–349.
- Lightfoot, M.D., Schumaker, S.A., Danczyk, S.A., Kastengren, A.L., 2015. Core Length and Spray Width Measurements in Shear Coaxial Rocket Injectors from X-ray Radiography Measurements (No. AFRL-RQ-ED-TP-2015-115). Air Force Research Lab, Edwards AFB, CA, Aerospace Systems Directorate.
- Linne, M., 2013. Imaging in the optically dense regions of a spray: a review of developing techniques. *Prog. Energy Combust. Sci.* 39 (5), 403–440.
- Linne, M.A., Paciaroni, M., Berrocal, E., Sedarsky, D., 2009. Ballistic imaging of liquid breakup processes in dense sprays. *Proc. Combust. Inst.* 32 (2), 2147–2161 II.
- Machicoane, N., Bothell, J.K., Li, D., Morgan, T.B., Heindel, T.J., Kastengren, A.L., Aliseda, A., 2019. Synchrotron radiography characterization of the liquid core dynamics in a canonical two-fluid coaxial atomizer. *Int. J. Multiphase Flow* 115, 1–8.
- Powell, C.F., Yue, Y., Poola, R., Wang, J., 2000. Time-resolved measurements of supersonic fuel sprays using synchrotron X-rays. *J. Synchrotron Radiat.* 7 (6), 356–360.
- Stevenin, C., Tomas, S., Vallet, A., Amielh, M., Anselmet, F., 2012. Shadowgraphy investigations of high speed water jet atomization into still air. ICLASS 2012, 12th Triennial International Conference on Liquid Atomization and Spray Systems Heidelberg, Germany, September.
- Westlye, F.R., Penney, K., Ivarsson, A., Pickett, L.M., Manin, J., Skeen, S.A., 2017. Diffuse back-illumination setup for high temporally resolved extinction imaging. *Appl. Opt.* 56 (17), 5028–5038.
- Van Wissen, R.J., Schreel, K.R., Van Der Geld, C.W., 2005. Particle image velocimetry measurements of a steam-driven confined turbulent water jet. *J. Fluid Mech.* 530, 353–368.
- Yue, Y., Powell, C.F., Poola, R., Wang, J.C., Schaller, J.K., 2001. Quantitative measurements of diesel fuel spray characteristics in the near-nozzle region using X-ray absorption. *At. Sprays* 11 (4), 471–490.